Article

Solvent Exsolution and Liberation from Different Heavy Oil–Solvent Systems in Bulk Phases and Porous Media: A Comparison Study

Wei Zou and Yongan Gu * [ID]

Petroleum Technology Research Centre (PTRC), Petroleum Systems Engineering, Faculty of Engineering and Applied Science, University of Regina, Regina, SK S4S 0A2, Canada; wzh349@uregina.ca
* Correspondence: peter.gu@uregina.ca; Tel.: +1-(306)-585-4630

Abstract: In this paper, experimental and numerical studies were conducted to differentiate solvent exsolution and liberation processes from different heavy oil–solvent systems in bulk phases and porous media. Experimentally, two series of constant-composition-expansion (CCE) tests in a PVT cell and differential fluid production (DFP) tests in a sandpacked model were performed and compared in the heavy oil–CO_2, heavy oil–CH_4, and heavy oil–C_3H_8 systems. The experimental results showed that the solvent exsolution from each heavy oil–solvent system in the porous media occurred at a higher pressure. The measured bubble-nucleation pressures (P_n) of the heavy oil–CO_2 system, heavy oil–CH_4 system, and heavy oil–C_3H_8 system in the porous media were 0.24 MPa, 0.90 MPa, and 0.02 MPa higher than those in the bulk phases, respectively. In addition, the nucleation of CH_4 bubbles was found to be more instantaneous than that of CO_2 or C_3H_8 bubbles. Numerically, a robust kinetic reaction model in the commercial CMG-STARS module was utilized to simulate the gas exsolution and liberation processes of the CCE and DFP tests. The respective reaction frequency factors for gas exsolution (rff_e) and liberation (rff_l) were obtained in the numerical simulations. Higher values of rff_e were found for the tests in the porous media in comparison with those in the bulk phases, suggesting that the presence of the porous media facilitated the gas exsolution. The magnitudes of rff_e for the three different heavy oil–solvent systems followed the order of $CO_2 > CH_4 > C_3H_8$ in the bulk phases and $CH_4 > CO_2 > C_3H_8$ in the porous media. Hence, CO_2 was exsolved from the heavy oil most readily in the bulk phases, whereas CH_4 was exsolved from the heavy oil most easily in the porous media. Among the three solvents, CH_4 was also found most difficult to be liberated from the heavy oil in the DFP test with the lowest rff_l of 0.00019 min^{-1}. This study indicates that foamy-oil evolution processes in the heavy oil reservoirs are rather different from those observed from the bulk-phase tests, such as the PVT tests.

Keywords: solvent exsolution and liberation; non-equilibrium phase behaviour; foamy-oil formation and flow; heavy oil–solvent systems; heavy oil reservoirs

1. Introduction

The primary productions in some heavy oil reservoirs exhibit anomalous characteristics, such as low producing gas–oil ratios (GORs), high oil production rates and recovery factors (RFs) [1]. These abnormal characteristics could be attributed to foamy-oil flow, which is an unusual two-phase flow of oil with dispersed gas [2]. After the primary production, solvent-based enhanced oil recovery (EOR) methods can be applied by injecting one or several solvents into the heavy oil reservoirs to reduce the heavy oil viscosity and continue the foamy-oil production. Two major non-equilibrium processes greatly affect the foamy-oil production: solvent exsolution and liberation, which are referred to as the foamy-oil formation and evolution. Therefore, it is of practical importance to study the foamy-oil formation and evolution in the heavy oil reservoirs.

Physically, the dissolved gas in the oil is exsolved in the form of microbubbles when the pressure is reduced below the so-called bubble-point pressure. The bubbles could be dispersed in the heavy oil for a long time due to its high viscosity. As the dispersed bubbles grow and coalesce, they gradually liberate from the foamy oil to form the free gas. Extensive experimental, numerical, and theoretical studies have been conducted to understand the processes and mechanisms involved in the foamy-oil formation and evolution. Several factors influencing the foamy-oil formation and evolution have been experimentally studied in bulk phases and porous media, including the dead heavy oil viscosity, solvent type, and concentration as well as pressure drawdown method and rate.

The experimental results in the bulk-phase tests show that foamy-oil stability increases as the viscosity of the dead heavy oil increases [2,3]. First, the high viscosity of the heavy oil reduces the gas diffusion rate, causing the microbubbles to grow slowly through mass transfer. Second, high viscosity also hinders bubbles from coalescing and liberating from the foamy oil. Thus, oil recovery can even increase with the increase in the heavy oil viscosity [4]. From an engineering point of view, however, an optimum heavy oil viscosity could exist to achieve the highest oil RF. Wu et al. conducted pressure depletion tests in a sandpacked model by using three heavy oil samples with different viscosities but at the same CO_2 concentration [5]. They found that the heavy oil sample with an intermediate viscosity gave the highest oil recovery. This was because the heavy oil with a lower viscosity had less stable foamy oil, whereas the heavy oil with a higher viscosity had a lower mobility. These counteracting effects on the oil recovery were also studied by utilizing a viscosity reducer in heavy oil [6,7]. It was found that the oil recovery factors were increased markedly with the increase of viscosity-reducer concentration in the low concentration range. This was attributed to the decreased oil viscosity and increased oil mobility. At higher concentrations of the viscosity reducer, however, the increase in the oil recovery was more gradual because the foamy oil was less stable [6].

In addition to the heavy oil viscosity, solvent type and concentrations also play critical roles in foamy-oil formation and evolution. Three common solvents, CH_4, C_3H_8, and CO_2 as well as their mixtures, are mostly used in the heavy oil–solvent systems. Sun et al. conducted a series of tests in a PVT cell to study the different foamy-oil evolution processes in the heavy oil–CH_4/C_3H_8/CO_2 systems [8]. They found that more gas was evolved in the heavy oil–CH_4 system than in the heavy oil–C_3H_8/CO_2 system at the same solvent molar concentration, which indicated that CH_4 bubbles were nucleated more readily. The larger difference between the two pressures, at which bubbles started to nucleate and liberate, was found in the heavy oil–CH_4 system, which indicated that CH_4 bubbles were more difficult to liberate from foamy oil. Zhou et al. performed pressure depletion tests in a sandpacked model by using CH_4, C_3H_8, and a mixture of CH_4 and C_3H_8 [9]. The foamy oil in the heavy oil–CH_4 system was also found more stable than those in the other two heavy oil–solvent systems. Furthermore, the amount of the dissolved gas in heavy oil also affects foamy-oil evolution. PVT tests show that the higher the initial solution GOR in a heavy oil–solvent system is, the longer the bubbles can be dispersed in the heavy oil [2]. This was attributed to a higher supersaturation in the system at a higher solvent concentration. A higher supersaturation can lead to more and smaller bubbles being generated. Experimental results from sandpacked tests also reveal the same trend between initial solution GOR and supersaturation as found in the PVT tests. In addition, it was found that a lower limit of the initial solution GOR exists in order to have the foamy oil [10].

Another essential factor in foamy-oil formation and evolution is pressure drawdown. Three pressure drawdown methods are typically adopted in the experimental studies with bulk phase and porous media: (a) constant pressure depletion rate [11]; (b) constant volume withdrawal rate [12,13]; and (c) constant pressure depletion stepsize [14]. The measured pressure vs. volume (P–V) data in the PVT tests could show different characteristics by using the different pressure drawdown methods. In particular, the measured P–V data with the volume withdrawal rate method could show a rebound region when the pressure reached the bubble-nucleation pressure due to a high bubble growth rate [15]. In

contrast, smooth P–V data are usually obtained by using the constant pressure depletion rate method [11]. The P–V data obtained by using the constant pressure depletion stepsize method could have one or two turning points, at which the bubble-point pressure or pseudo bubble-point pressure was achieved [14]. How fast the pressure was reduced affects the gas exsolution and liberation processes. Experimental results show that as the pressure depletion rate was increased, the volume of dispersed gas and the duration in which gas bubbles were dispersed in the oil also were increased [11]. This is attributed to two reasons. First, a higher depletion rate leads to an insufficient time for bubbles to nucleate and thus lowers the pressure at which bubbles start to liberate to form the free gas. Second, a higher depletion rate results in a higher supersaturation and a higher bubble nucleation rate so that the bubbles nucleated can also be smaller [2].

Many theoretical models have been proposed to describe the foamy-oil formation and/or evolution processes. These models can be broadly categorized into two types: physics-based models [16,17] and kinetic reaction models [18–20]. In the physics-based models, bubble nucleation was considered as either progressive nucleation or instantaneous nucleation. Progressive nucleation has been modeled by using the classic bubble nucleation theory or the pre-existing bubble theory [21,22]. In instantaneous nucleation, bubbles are nucleated instantaneously and no more new bubbles are nucleated [23]. The bubble number at the onset of bubble nucleation is assigned an initial guessing value and then adjusted to match the calculated data with the measured data. The bubble growth was controlled by mechanic expansion and mass transfer [4,23]. For the bubble liberation, some empirical correlations are made available in the literature and have been verified by limited experimental data. The kinetic reaction models are developed from chemical kinetics theories and assume that three or more gas components exist in the foamy-oil formation and evolution. Typically, the gas components include the solution gas, dispersed gas, and free gas [24–26]. The dispersed gas and free gas together are also referred to as the evolved gas. The reaction rate of a gas component transferring to another gas component is assumed to be proportional to the concentration of the reactant gas component. The kinetics model proposed by Coombe and Maini [27] has been used in the CMG-STARS module since it is predictive and can simulate the time-dependent phenomena [28].

Although numerous studies have investigated the foamy-oil formation and/or evolution in the porous media or bulk phases alone, few studies have focused on studying the effects of the bulk phases and porous media on the foamy-oil formation and evolution processes in different heavy oil–solvent systems. The research results obtained in the bulk phases and porous media could be different and cause confusion in the heavy oil industry. Hence, it is important to understand their differences prior to the oil field applications. In this paper, three constant-composition-expansion (CCE) tests in a PVT cell and three differential fluid production (DFP) tests in a sandpacked model were conducted in the heavy oil–CO_2, heavy oil–CH_4, and heavy oil–C_3H_8 systems. The total isothermal compressibility (c_t) vs. test pressure (P) data were measured in all the tests, while the oil and gas production data were also measured in the tests in the porous media. Afterwards, numerical simulations were executed to simulate the six tests. From these simulations, two reaction frequency factors were obtained to quantify the foamy-oil formation and evolution processes. The results from the experimental tests and numerical simulations in this study provide insights into the differences of foamy-oil formations and evolutions in the bulk phases and porous media.

2. Experimental

2.1. Materials

The heavy oil sample (Well No.: 16A-3-59-7) used in this study was collected from the Colony formation in the Bonnyville area, Alberta, Canada. Prior to the measurements of the heavy oil properties, the heavy oil was centrifuged to remove the possibly existing sands and/or brine from the oil. The compositions of the Colony heavy oil were measured by using the standard ASTM D86 and are given in Table 1. It can be seen from the table

that the minimum carbon number of the Colony heavy oil was C_9 and that the hydrocarbons were measured up to C_{60}. The heavy oil density and viscosity were measured to be $\rho_o = 0.992$ g/cm^3 and $\mu_o = 33{,}876$ cP by using a densitometer (DMA 4200, Anton Paar, Graz, Austria) and a viscometer (DV-II+, Brookfield Engineering, Middleboro, MA, USA) at $P_a = 1$ atm and $T_{lab} = 21°$ C, respectively. The respective measured densities and viscosities of the Colony heavy oil at $P_a = 1$ atm and different temperatures are listed in Table 2. Both the density and viscosity of the heavy oil decrease with the increase in temperature. The molecular weight of the heavy oil was measured to be $MW_o = 547.7$ g/mol by using an automatic high-sensitivity wide-range cryoscopy (Model 5009, Precision Systems Inc., Natick, MA, USA). The asphaltene content of the heavy oil was measured to be $W_{asp} = 18.3$ wt.% (*n*-C_5 insoluble) by using the standard ASTM D2007-19 method. Three solvents used in this study, CO_2, CH_4, and C_3H_8, were purchased from Linde Canada Inc. (Mississauga, ON, CA) and had purities of 99.998 mol.%, 99.97 mol.%, and 99.5 wt.%, respectively.

Table 1. Compositional analysis result of the Colony heavy oil (Well No.: 16A-3-59-7) collected from the Bonnyville area, Alberta [29].

Carbon no.	mol.%	wt.%	Carbon no.	mol.%	wt.%
C_1	0.00	0.00	C_{32}	1.46	1.61
C_2	0.00	0.00	C_{33}	1.32	1.50
C_3	0.00	0.00	C_{34}	1.28	1.50
C_4	0.00	0.00	C_{35}	1.15	1.39
C_5	0.00	0.00	C_{36}	1.05	1.30
C_6	0.00	0.00	C_{37}	1.16	1.48
C_7	0.00	0.00	C_{38}	1.00	1.31
C_8	0.00	0.00	C_{39}	0.99	1.33
C_9	0.79	0.25	C_{40}	1.05	1.45
C_{10}	2.61	0.91	C_{41}	0.93	1.32
C_{11}	2.21	0.85	C_{42}	0.98	1.42
C_{12}	3.80	1.59	C_{43}	1.06	1.57
C_{13}	4.20	1.90	C_{44}	0.96	1.45
C_{14}	4.51	2.19	C_{45}	0.89	1.39
C_{15}	4.49	2.34	C_{46}	0.83	1.32
C_{16}	4.67	2.59	C_{47}	0.77	1.25
C_{17}	4.43	2.61	C_{48}	0.67	1.11
C_{18}	4.18	2.61	C_{49}	0.55	0.93
C_{19}	3.87	2.55	C_{50}	0.64	1.11
C_{20}	3.52	2.44	C_{51}	0.63	1.11
C_{21}	3.16	2.30	C_{52}	0.51	0.92
C_{22}	2.99	2.28	C_{53}	0.40	0.74
C_{23}	2.54	2.02	C_{54}	0.53	0.99
C_{24}	2.47	2.05	C_{55}	0.47	0.89
C_{25}	2.21	1.91	C_{56}	0.53	1.03
C_{26}	2.22	2.00	C_{57}	0.40	0.78
C_{27}	2.24	2.09	C_{58}	0.44	0.88
C_{28}	1.89	1.83	C_{59}	0.39	0.79
C_{29}	1.97	1.98	C_{60}	0.35	0.72
C_{30}	1.68	1.74	C_{61+}	8.53	20.85
C_{31}	1.43	1.53	Total	100.00	100.00

Table 2. The Colony heavy oil densities (ρ_o) and viscosity (μ_o) at P_a = 1 atm and different temperatures.

T (°C)	ρ_o (g/cm^3)	μ_o (cP)
21	0.9920	33,876
30	0.9864	10,539
40	0.9804	3,980
50	0.9743	1,679
60	0.9681	795.9

2.2. Experimental Setup and Procedures for the CCE Tests

In this study, three CCE tests were carried out by using a mercury-free PVT system (PVT-0150-100-200-316-155, DBR, Canada), as schematically shown in Figure 1. The PVT system was mainly composed of a PVT cell, an air bath, an oil injection unit, and a digital image-based height measurement system. The see-through PVT cell was a glass tube with an inner diameter (ID) of 1.252 inches and a length of 8.005 inches. A freely movable piston was positioned in the PVT cell to pressurize the test fluids. The PVT cell can withstand a high pressure up to 69 MPa and a high temperature of 200.0 °C. A syringe pump (100 DX, Teledyne ISCO, Lincoln, NE, USA) connected to the PVT cell was used to apply the test pressure and overburden pressure to the PVT cell. The test temperature can be controlled by using an air bath, which is surrounded by the PVT cell. The oil injection unit consisted of a high-pressure transfer cylinder and another syringe pump (500 DX, Teledyne ISCO, Lincoln, NE, USA). The high-pressure transfer cylinder held the solvent-saturated live oil, and the syringe pump was used to inject the solvent-saturated live heavy oil into the PVT cell. The digital image-based height measurement system included a high-resolution color monitor, a cathetometer, and an encoder. The image of the piston or fluid interface (s) in the PVT cell can be viewed and captured by the camera and displayed on the monitor. The encoder was used to adjust and record the height of the piston or fluid interface (s). The height measurement resolution of the system was 0.001 inches.
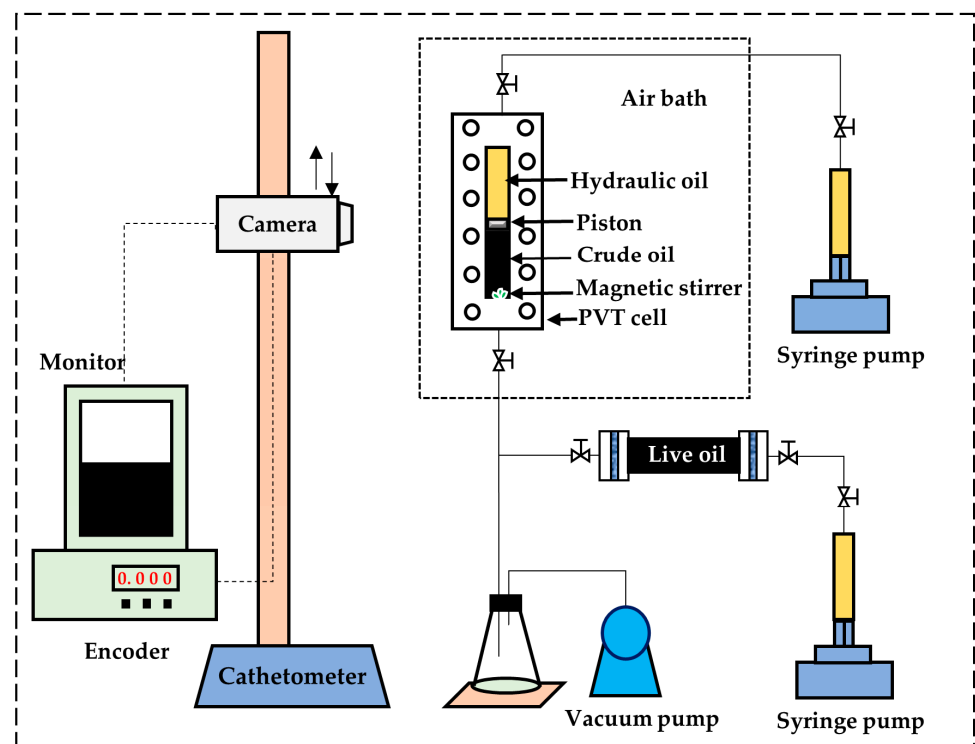
Figure 1. Schematic diagram of the experimental setup for conducting the CCE tests [30].

The three CCE tests for the three heavy oil–solvent systems were conducted by using the following experimental procedures:

(1) The $CO_2/CH_4/C_3H_8$-saturated heavy oil was prepared by mixing a solvent ($CO_2/CH_4/C_3H_8$) and the dead Colony heavy oil in two high-pressure transfer cylinders. The mixture in the two high-pressure transfer cylinders was pumped back and forth for about 15–20 days until the target GOR of the live oil was achieved. The solvent concentrations (C_s) in the prepared heavy oil–CO_2 system, heavy oil–CH_4 system and heavy oil–C_3H_8 system were measured and are listed in Table 3.

(2) The PVT cell was cleaned with kerosene and ethanol and then air-dried for 24 h. A leakage test was conducted by injecting CO_2 into the PVT cell at a constant pressure of 3.5 MPa. The PVT cell was considered leakage-free if the pressure reduction was less than 5 psi after 24 h. Then, the CO_2 in the cell was released to an exhaust ventilation hose. Afterwards, a vacuum pump was used to vacuum the PVT cell.

(3) The piston in the PVT cell was pushed to the bottom of the PVT cell. The PVT cell pressure and its overburden pressure were raised to a pressure higher than the bubble-point pressure of the live oil by using the ISCO pump, which was connected to the PVT cell and its overburden chamber. Then, a pre-specified volume of the live oil (V_{oi}) was injected into the PVT cell by using another syringe pump. The volumes of the injected three live oils in the three CCE tests (Tests #1, #3 and #5) are given in Table 3.

(4) The PVT cell pressure was reduced stepwise by using a pre-specified pressure step (ΔP) given in Table 3. The height (H) of the test fluid column in the PVT cell and the volume of the syringe pump connected to the PVT cell were monitored and recorded every 10 min.

(5) The total test-fluid volume (V_t) in the PVT cell, total isothermal compressibility (c_t) and relative volume (R_v) were measured when the volume change of the syringe pump was less than 0.12 cc within 10 min. Here, V_t, c_t and R_v are defined as

$$V_t = \frac{\pi D^2}{4} \cdot H - V_{dv} \tag{1}$$

$$c_t = -\frac{1}{Vt}\left(\frac{\Delta Vt}{\Delta P_{cell}}\right)_T \tag{2}$$

$$R_v = \frac{Vt}{V_{oi}} \tag{3}$$

where D and H are the ID of the PVT cell glass tube and the height of the test fluid column in the PVT cell; V_{dv} is the dead volume in the PVT cell; ΔV_t is the change of total test-fluid volume caused by the change of the PVT cell pressure (ΔP_{cell}); and V_{oi} is the volume of the live oil that was initially injected into the PVT cell.

(6) Steps 4 and 5 were repeated until the PVT cell pressure reached a pre-specified test termination pressure.

Table 3. Test details, measured data, and tuned reaction frequency factors of Tests #1–6.

Test No.	Test	C_s (mol.%)	V_{oi} (cm³)	ϕ (%)	k (D)	S_{oi} (%)	ΔP (MPa)	P_b (MPa)	P_n (MPa)	rff_e (min⁻¹)	rff_1 (min⁻¹)
1	CO₂-CCE	27.66	39.78	-	-	-	0.20	2.00	1.73	0.00052	-
2	CO₂-DFP		-	40	2.6	98			1.97	0.00075	0.009
3	CH₄-CCE	11.32	38.51	-	-	-	0.20	1.70	0.60	0.00009	-
4	CH₄-DFP		-	39	2.7	97			1.50	0.013	0.00019
5	C₃H₈-CCE	27.31	40.54	-	-	-	0.05	0.50	0.48	0.0001, 0.000065	-
6	C₃H₈-DFP		-	39	1.9	97			0.50	0.00025	0.0045

2.3. Experimental Setup for the DFP Tests

The experimental setup for conducting the three DFP tests mainly consisted of four operating units: a 2-D rectangular sandpacked physical model; a water/oil injection module; a fluids production system; and a data acquisition system (DAS). The schematic diagram of the experimental setup for conducting the three DFP tests is shown in Figure 2. The physical model was composed of four parts: a stainless-steel base; a thin polycarbonate plate; a thick transparent acrylic plate; and a stainless-steel cover. The stainless-steel base had a rectangular cavity with the dimensions of 40 cm $\times$ 10 cm $\times$ 2 cm for packing the sand grains. The polycarbonate plate was placed between the stainless-steel base and the acrylic plate to avoid scratching on the latter. The stainless-steel cover was used to place and secure the stainless-steel base, the polycarbonate plate, and the acrylic plate together. The physical model has two ports at its two ends. The one on the right-hand side was used as a reservoir fluids producer in each test. The other, on the left-hand side, was used to inject water/oil and establish the initial water/oil saturation.
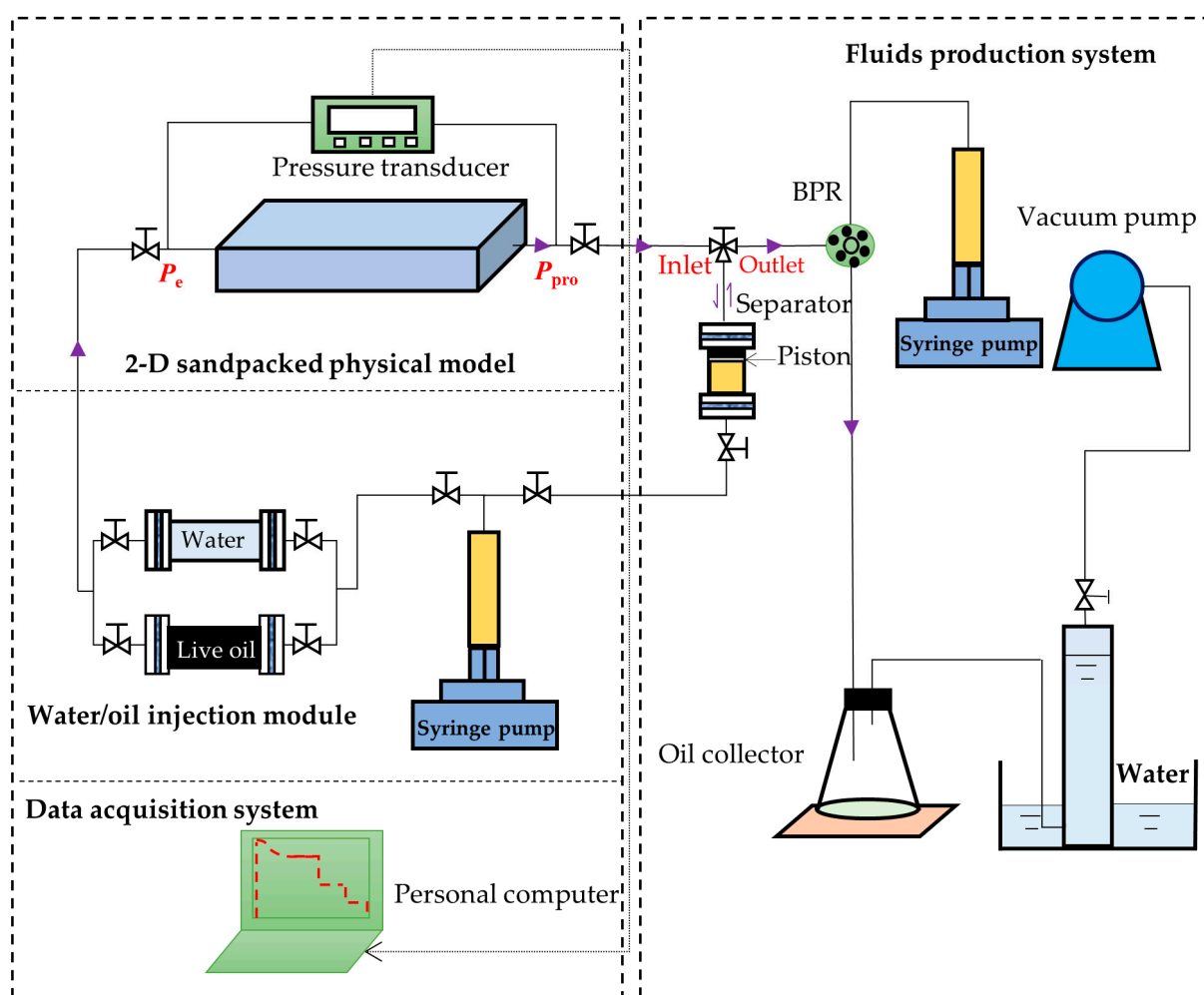
Figure 2. Schematic diagram of the experimental setup for conducting the DFP tests.

The water/oil injection module comprised two high-pressure transfer cylinders and a syringe pump (500 D, ISCO Inc., USA). One transfer cylinder held the de-ionized water and the other contained the solvent-saturated live heavy oil. Along the produced reservoir fluids flow direction, the fluids production system was composed of a high-pressure transfer cylinder with a freely movable piston used as a separator, a high-precision back-pressure regulator (BPR, LBS4 Series, Swagelok, Solon, OH, USA), a glass flask, an electronic scale, and a gas bubbler. The separator's bottom port was connected to the syringe pump (500 D, Teledyne ISCO, Lincoln, NE, USA) used in the water/oil injection module, while its top port

was connected to the common port of an L-type three-way valve. The three-way valve's inlet port was connected to the sandpacked model and its outlet port was connected to the BPR. The BPR was connected to a different syringe pump (260 D, Teledyne ISCO, Lincoln, NE, USA) to maintain its back pressure. After the BPR, the glass flask, electronic scale, and bubbler were used to collect the produced dead oil, measure its mass, and measure the produced gas volume at the atmospheric conditions, respectively. The DAS mainly consisted of two high-precision pressure transducers (PXM409, Omegadyne Inc., Sunbury, OH, USA) at the two ends of the physical model to measure the two pressures at any time during each test. The pressure data were recorded and stored in a personal computer, to which the pressure transducers were connected. The respective pressures measured at the fluids production end on the right-hand side and at the other end on the left-hand side were denoted by P_{pro} and P_e.

The DFP tests were conducted by using the following experimental procedures:

(1) The sieved sand grains (Bell & Mackenzie, Toronto, ON, Canada) with sizes of 60–80 mesh were added into the physical model through one of its ports. The sand-packed model was hammered continuously by using a rubber hammer until no void space existed in the model.

(2) The leakage test was conducted by injecting CO_2 into the sandpacked model at 3 MPa for each DFP test. The sandpacked model was considered leakage-free if its pressure reduction was less than 0.2 MPa within 24 h.

(3) The porosity (ϕ) and permeability (k) measurements were performed by using the imbibition method and the Darcy's law, respectively. The measured permeabilities and porosities of the three DFP tests (Tests #2, #4, #6) are listed in Table 3.

(4) Water was injected into the 2-D physical model first to raise the reservoir pressure higher than the bubble-point pressure of the live heavy oil. Then the solvent-saturated live oil was injected to displace the water until no more water was produced from the 2-D physical model and the measured solution GOR reached the initial solution GOR. The initial oil saturations (S_{oi}) were determined by using the material balance equation and are given in Table 3.

(5) The separator (i.e., a high-pressure cylinder) was connected to the 2-D physical model after its pressure was increased to the reservoir pressure. A period of 24 h was allowed for the 2-D physical model and separator to reach an equilibrium state.

(6) The separator and reservoir pressures were reduced simultaneously by applying a pre-specified pressure depletion stepsize (ΔP). The produced fluids (heavy oil and/or gas) were collected in the separator and their total volume (V_f) at the separator pressure was monitored and recorded by using a syringe pump. The pressures at the two ends of the sandpacked physical model (P_{pro} and P_e) were monitored and recorded.

(7) The production data, including P_{pro} and P_e, were measured when the pump volume change was less than 0.12 cc within 10 min. First, the three-way valve was switched to disconnect the separator from the physical model and the produced fluids in the separator were displaced to measure the dead-oil and gas volumes (V_{do} and V_g) at the atmospheric pressure. Second, the volumes of the cumulative produced fluids at the reservoir conditions (Q_f), cumulative produced dead oil and gas (Q_o and Q_g) at the atmospheric conditions, as well as the total isothermal compressibility (c_t), were measured with the following equations:

$$Q_f = \sum V_f \tag{4}$$

$$Q_o = \sum V_o \tag{5}$$

$$Q_g = \sum V_g \tag{6}$$

$$c_t = -\frac{1}{PV}\left(\frac{V_f}{\Delta P_{res}^{ave}}\right)_T \tag{7}$$

where PV and $\Delta P_{\text{res}}^{\text{ave}}$ represent the pore volume of the physical model and the change of the average reservoir pressure, $P_{\text{res}}^{\text{ave}} = (P_{\text{pro}} + P_{\text{e}})/2$.

(8) Each DFP test was continued by repeating Steps 6 and 7 until the production pressure reached a pre-specified ending production pressure, e.g., P_{pro} =0.8, 0.3, and 0.3 MPa in the heavy oil–CO_2 system, heavy oil–CH_4 system, and heavy oil–C_3H_8 system, respectively.

3. Numerical Modeling

Numerical simulations were undertaken by using the CMG simulator to simulate the experimental tests in order to obtain the quantitative results of the foamy-oil formations and evolutions in the three heavy oil–solvent systems with or without the porous media. The fluid models were built in the CMG-WinProp module by matching the measured dead oil and live oil properties. The CMG-STARS module with the foamy-oil kinetic reaction model was utilized to history match the relative volume vs. test pressure data in the CCE tests and the production data in the DFP tests.

3.1. Fluid Models

In this work, the fluid models for the three heavy oil–solvent systems were generated by using the Peng–Robinson equation of state (PR-EOS) in the CMG-WinProp module. The components of the heavy oil listed in Table 1 were lumped into two pseudo-components: 9.59 mol.% C_{9-12} and 90.41 mol.% C_{13+}. The related physicochemical properties of the two pseudo-components were used as the adjustable parameters to match the measured densities and viscosities at P_{a} = 1 atm and different temperatures in Table 2. The tuned physicochemical properties of the two pseudo-components of the Colony heavy oil are given in Table 4. Afterwards, a solvent (CO_2/CH_4/C_3H_8) was added into the two pseudo-components and the measured live-oil bubble-point pressures in Table 3 were matched to generate the CO_2/CH_4/C_3H_8-saturated fluid models. The tuned corresponding binary interaction parameters (BIPs) between each solvent and the two pseudo-components are listed in Table 4.

Table 4. Physicochemical properties of the two pseudo-components of the Colony heavy oil and their respective binary interaction parameters (BIPs) with CO_2/CH_4/C_3H_8.

Properties and BIPs	Two Pseudo-Components	
	C_{9-12}	C_{13+}
Critical pressure P_{c} (MPa)	2.33	0.69
Critical temperature T_{c} (K)	642.86	938.31
Pitzer acentric factor ω	0.4789	0.9805
Molecular weight MW (g/mol)	146.9	596.7
BIP with CO_2	0.12	0.14
BIP with CH_4	0.045	0.085
BIP with C_3H_8	0.036	0.106

3.2. Numerical Simulations of the CCE and DFP Tests

The CMG-STARS module was employed as a thermal compositional simulator to simulate the measured relative volume data in the three CCE tests (Tests #1, #3, and #5). The numerical simulations of the CCE tests using the CMG-STARS module in this study were similar to those conducted before [31]. The cylindrical PVT cell in each CCE test was modeled by building a simulation model with $1 \times 1 \times 4$ grid blocks along the x, y and z directions, as shown in Figure 3. Initially, the two upper grid blocks (1, 1, 1) and (1, 1, 2) had the live heavy oil only, whereas the two lower grid blocks (1, 1, 3) and (1, 1, 4) had

water only. In order to simulate the CCE tests in the CMG-STARS module, an extremely high porosity of $\phi = 0.99$ and an absolute permeability of $k = 10,000$ D were assigned to the four grid blocks. The dimensions of the simulation model in its x and y directions were 2.83×2.83 cm^2 so that its horizontal cross-sectional area was almost the same as that of the PVT cell (ID = 3.18 cm) after the porosity (ϕ) was considered. The thicknesses of the two upper grid blocks (1, 1, 1) and (1, 1, 2) were the same and were determined by the volume of the injected live oil in each CCE test. Therefore, the two upper grid blocks (1, 1, 1) and (1, 1, 2) had the same thickness of 2×2.50, 2×2.42 and 2×2.55 cm for the heavy oil–CO_2 system ($V_{oi} = 39.78$ cm^3), heavy oil–CH_4 system ($V_{oi} = 38.51$ cm^3) and heavy oil–C_3H_8 system ($V_{oi} = 40.54$ cm^3), respectively. The thicknesses of the two lower grid blocks (1, 1, 3) and (1, 1, 4) were equal to 5.00 cm for all three heavy oil–solvent systems. A vertical producer was drilled from the top grid block to the bottom grid block but only the bottom grid block (1, 1, 4) was perforated. In this way, the simulation model pressure could be controlled by the vertical producer at the top of the simulation model. The water was produced as the simulation model pressure was reduced. The volume of the produced water at the reservoir conditions was equivalent to the expanded total volume of the test fluids. Hence, the relative volume (R_v) in the CCE tests can be simulated by using the CMG-STARS module. It is worthwhile to note that the water compressibility was set to be zero to eliminate its effect on the produced water volume.
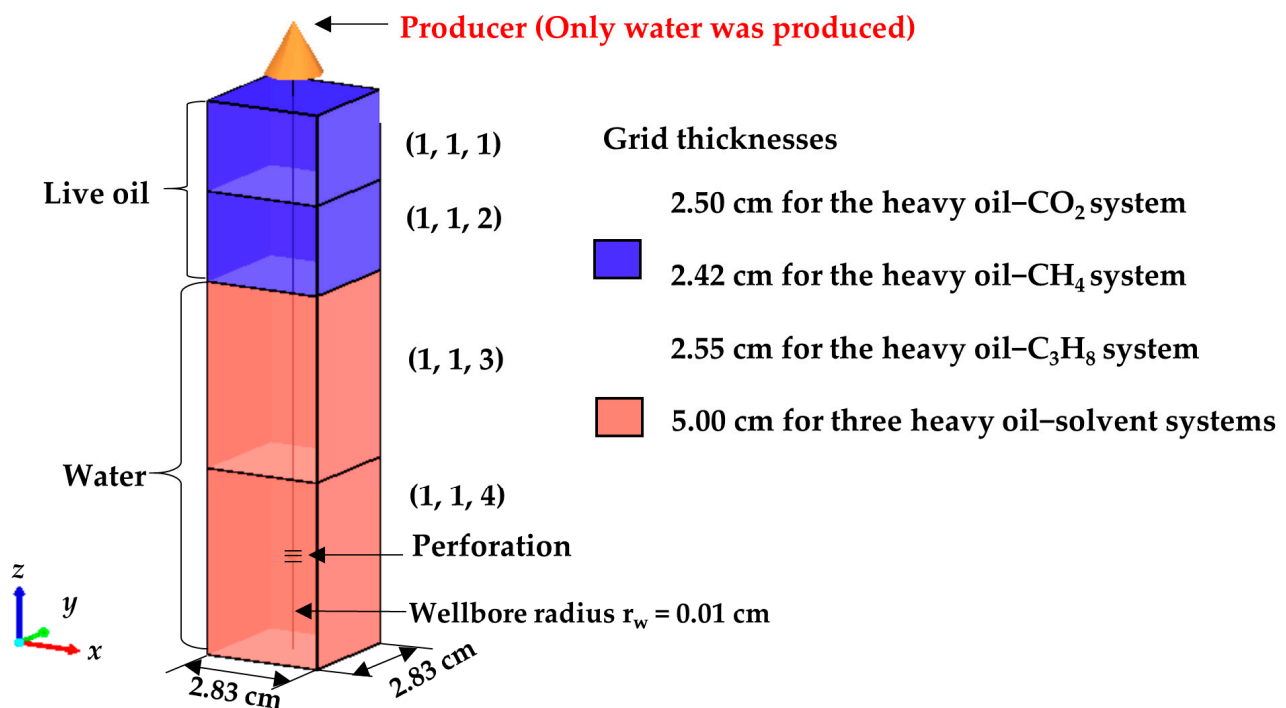
Figure 3. Three-dimensional view of the rectangular simulation model with four grid blocks for the CCE tests.

In the numerical simulations conducted by before [31], the relative permeability curves were altered to prevent oil and gas from moving between the grid blocks. In this study, however, three sets of relative permeability data were used for different grid blocks in order to improve the convergence of numerical simulation. In grid blocks (1, 1, 1) and (1, 1, 2), the oil and gas components had high relative permeabilities. Grid block (1, 1, 3) was set as a transition zone, in which all the components could move and the relative permeabilities of the oil and water were proportional to their corresponding saturations in the liquid phase. In grid block (1, 1, 4), the water relative permeability was set to be extremely high, whereas the oil and gas relative permeabilities were set to be extremely low so that only the water in the grid block (1, 1, 4) could be produced but the oil and gas could not. Therefore,

the overall composition of all the test fluids (heavy oil + gas) remained constant in the numerical simulation. The three sets of relative permeability data are listed in Table 5.

Table 5. Three sets of relative permeability data used in different grid blocks.

Grid Block	Liquid Saturation and Relative Permeability		
	S_w [a]	k_{rw} [b]	k_{row} [c]
	0	0	1
	1.0×10^{-5}	0	1
	0.97999	0	1
(1, 1, 1) and (1, 1, 2)	1	1	0
	S_l [d]	k_{rg} [e]	k_{rog} [f]
	0	1	0
	1.0×10^{-5}	1	1
	0.9999	1	1
	1	0	1
	S_w	k_{rw}	k_{row}
	0	0	1
	1	1	0
	S_l	k_{rg}	k_{rog}
(1, 1, 3)	0	1	0
	1.0×10^{-5}	1	1
	0.9999	1	1
	1	0	1
	S_w	k_{rw}	k_{row}
	0	0	1.0×10^{-9}
	0.1	1	0
(1, 1, 4)	1	1	0
	S_l	k_{rg}	k_{rog}
	0	1.0×10^{-9}	0
	1	0	1.0×10^{-9}

Notes: [a] Water saturation; [b] Relative permeability to water at S_w; [c] Relative permeability to oil at S_w. [d] Liquid saturation; [e] Relative permeability to gas at S_l; [f] Relative permeability to oil at S_l.

Similar to the CCE tests, three DFP tests (Tests #2, #4, and #6) were also simulated by using the CMG-STARS module. The simulation model had $40 \times 5 \times 1$ grid blocks with the dimensions $40 \times 10 \times 2$ cm^3 in the x, y, and z directions. The model's porosities and permeabilities in the x, y, and z directions were assumed to be uniform and the same as those of the DFP tests. The initial reservoir conditions were also set to be the same as those in the DFP tests. The oil–water and liquid–gas relative permeabilities were first generated by using the modified Brooks–Corey correlations [32] and then adjusted by matching the predicted production data (i.e., P_e, Q_o, Q_g, Q_f) from the CMG-CMOST module to those measured production data in the DFP tests.

3.3. Foamy-Oil Kinetic Reaction Model

Foamy oil was simulated in the CMG-STARS module by using the entrained-gas model. The entrained-gas model includes two kinetic reactions, which describe the gas

exsolution and liberation processes, respectively. The reaction rates of gas exsolution and liberation are expressed as follows [33]:

$$r_e = rff_e \cdot \exp\left(-\frac{E_a}{RT}\right) \cdot \phi \cdot S_{fo} \cdot n_{fo} \cdot (x - x_{eq}), \tag{8}$$

$$r_l = rff_l \cdot \exp\left(-\frac{E_a}{RT}\right) \cdot \phi \cdot S_{fo} \cdot n_{fo} \cdot x_{bub}, \tag{9}$$

where r denotes the reaction rate per bulk volume in mol/(min·cm^3); rff denotes the reaction frequency factor in 1/min; the subscripts e and l represent gas exsolution and liberation, respectively. E_a is the activation energy in J/mol; R is the universal gas constant of 8.3145 J/(mol· K); T is the reaction temperature in K; ϕ is the porosity; S_{fo} is the foamy-oil saturation in fraction; n_{fo} is the molar density of the foamy oil in mol/cm^3; x, x_{eq} and x_{bub} are the mole fractions of the dissolved gas, the dissolved gas at the equilibrium state and the dispersed bubble in the foamy oil. Since the DFP tests were conducted at the constant temperature of 21 °C, the activation energy E_a was set to be zero [34,35]. Hence, only the reaction frequency factors (rff_e and rff_l) in Equations (8) and (9) need to be determined.

Physically, $(x - x_{eq})$ in Equation (8) represents the deviation of the dissolved gas mole fraction from its equilibrium value at the existing test pressure. The x_{eq} can be calculated from the equilibrium constant (K-value) generated from the CMG-WinProp module. The higher $(x - x_{eq})$ is, the higher supersaturation in the live oil. The rff_e can be used to compare how fast the dissolved gas was exsolved to form dispersed gas in two systems at the same supersaturation. Similarly, rff_l in Equation (9) indicates how fast the dispersed gas is liberated from the foamy oil to form free gas. In the numerical simulations, the reaction rates of gas exsolution and liberation can be calculated with the two factors (rff_e and rff_l) by using Equations (8) and (9) once $(x - x_{eq})$ becomes greater than zero due to supersaturation. Then, the calculated reaction rates could be easily incorporated into the existing continuity equations with the mass-transfer terms in the CMG-STARS module.

4. Results and Discussion

4.1. Heavy Oil–CO$_2$ System

In this study, the equilibrium CCE data, namely the R_v vs. P_{cell} data, were predicted by using the PR-EOS in the CMG-WinProp module. The non-equilibrium R_v vs. P_{cell} data were predicted by using the CMG-STARS module. Figure 4 compares the predicted equilibrium R_v vs. P_{cell} data with the measured and predicted non-equilibrium R_v vs. P_{cell} data of Test #1 for the heavy oil–CO$_2$ system. It can be seen from the figure that the predicted equilibrium R_v vs. P_{cell} data had an obvious turning point at P_{cell} = 2.00 MPa, which was called the bubble-point pressure (P_b) of the heavy oil–CO$_2$ system. It can be seen from the predicted equilibrium R_v vs. P_{cell} data that the total volume of the test fluids (the heavy oil and gas) increased drastically once the test pressure was reduced to below P_b. In contrast, the measured non-equilibrium R_v vs. P_{cell} data did not show a noticeable change until P_{cell} = 1.73 MPa, at which a certain amount of the bubbles were nucleated. In this study, this threshold pressure was called the bubble-nucleation pressure (P_n), i.e., $P_n = P_{cell}$ = 1.73 MPa.

Here, P_n was used for the non-equilibrium tests to distinguish it from P_b, which was defined at the equilibrium state. Supersaturation started to occur in the live heavy oil at $P_{cell} < P_b$ and was the driving force for the bubble nucleation [36]. The bubbles could not be nucleated until a certain degree of supersaturation was reached, which is defined as the critical supersaturation (P_{crit}), namely, the pressure difference between P_b and P_n in this study.

Figure 4 also shows that an increased relative volume at each pressure drop was much smaller at $P_{cell} < P_n$ = 1.73 MPa at the non-equilibrium state than that at $P_{cell} < P_b$ = 2.00 MPa at the equilibrium state. This difference was attributed to the relatively smaller amount

of the gas that was exsolved in the non-equilibrium state than that in the equilibrium. It was difficult to reach the equilibrium state in a heavy oil–solvent system during a CCE test due to the low bubble nucleation rate and CO_2 diffusion rate in the heavy oil [37]. The predicted non-equilibrium R_v vs. P_{cell} data from the CMG-STARS module are also plotted in Figure 4 after history matching the measured R_v vs. P_{cell} data. The predicted non-equilibrium relative volume data matched well with the measured data. The value of rff_e in Equation (8) was tuned to be 0.00052 min^{-1}. The rff_1 in Equation (9) was not obtained in the CMG-STARS module for the CCE tests. This was because the keyword *GASSYLIQ was used in the simulation module to give the same isothermal compressibility of the dispersed gas as that of the free gas [38]. This means that the system's total isothermal compressibility was determined by the total amount of the dispersed gas and free gas (i.e., the evolved gas) and thus was irrelevant to the individual amount of either gas. In this case, the tuned rff_e was sufficient to calculate the amount of the evolved gas and match the total volume changes measured in the CCE tests.
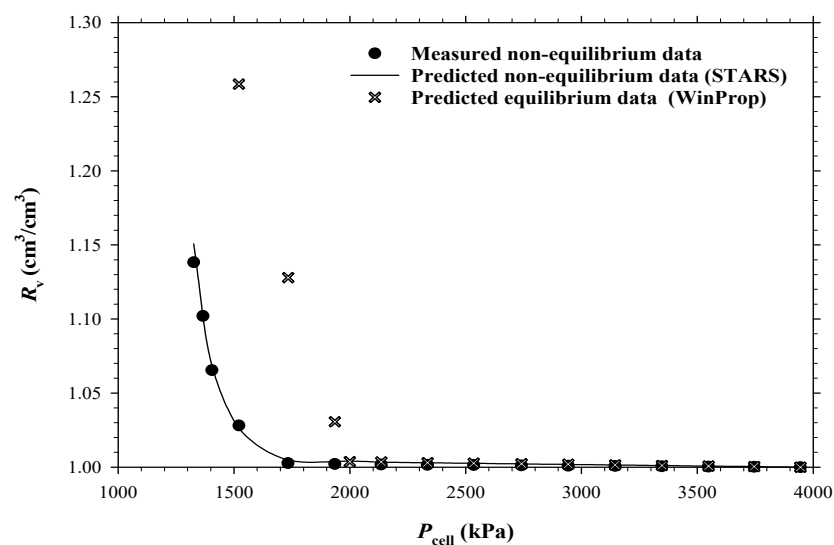
Figure 4. Measured and predicted non-equilibrium relative volume (R_v) vs. PVT cell pressure (P_{cell}) data as well as predicted equilibrium R_v vs. P_{cell} data in Test #1 for the heavy oil–CO_2 system.

Test #2 was conducted to study the gas exsolution in the porous media. Figure 5 depicts the measured and predicted production data (P_e, Q_o, Q_g, Q_f) of Test #2. As shown in the figure, P_e decreased quickly and the slopes of Q_o, Q_g, and Q_f were almost constant at $P_e > P_n$. This was because the reservoir fluids in the sandpacked model were still in the liquid phase. When P_e was slightly lower than P_n, P_e was reduced more slowly, indicating the existence of bubbles in the sandpacked model. This was because the gas phase had a much higher compressibility than that of the liquid phase and thus could much better help to maintain the reservoir pressure. The absolute slope of Q_o was decreased at $P_e < P_n$. This was because the CO_2-diluted heavy oil had a relatively lower viscosity at $P_e > P_n$. The viscosity of the CO_2-diluted heavy oil was drastically increased after the dissolved gas was exsolved from the live oil, causing a lower oil production rate. As P_e continued to decrease, the absolute slope of Q_o did not change much initially and then started to decrease due to the free-gas production.

The total isothermal compressibilities (c_t) measured in Tests #1 and #2 are compared in Figure 6. Two turning points were found and three regions (Regions I, II, and III) could be identified in each dataset. In Region I, the compressibility data were low and remained almost constant. This region represented the single liquid phase. In Region II, bubbles started to be nucleated and the total isothermal compressibilities of the two tests were increased accordingly. The measured bubble-nucleation pressures (P_n) were found to be 1.73 MPa in Test #1 and 1.97 MPa in Test #2 from Figure 6. Therefore, the supersaturation at

P_n in Test #1 was higher than that in Test #2. The main reason for the lower supersaturation in Test #2 was the presence of the porous media in the test. The sand grains in Test #2 provided tremendous bubble nucleation sites for bubbles to nucleate easily and thus decreased the supersaturation needed for the bubble nucleation [39]. The numerical simulation results are consistent with the experimental results. It was found that the values of rff_e obtained from Tests #1 and #2 were 0.00052 min^{-1} and 0.00075 min^{-1}, respectively. A higher rff_e indicated that the dissolved gas was more readily exsolved, to form gas bubbles and/or diffuse into the existing gas bubbles in Test #2 with the porous media.
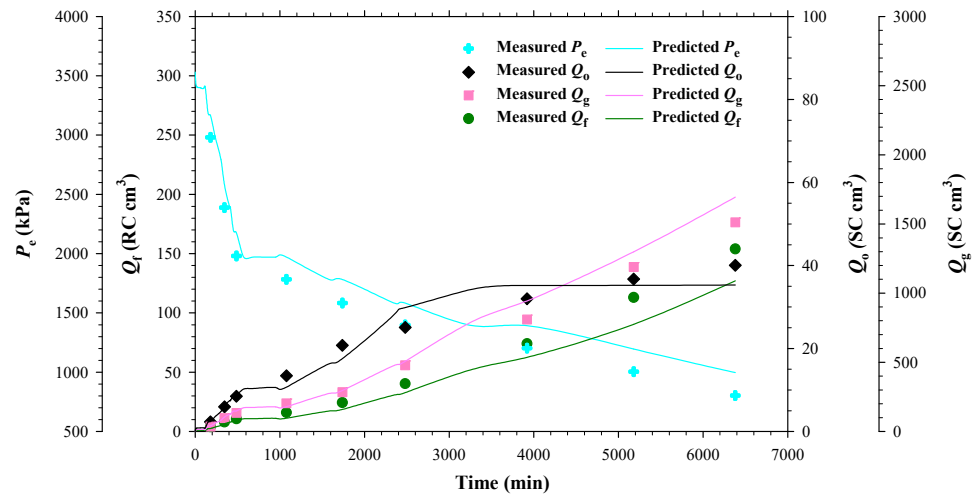
Figure 5. Measured and predicted pressures at the opposite end of the producer (P_e); cumulative total fluids production (Q_f) at the reservoir conditions; cumulative oil and gas productions (Q_o and Q_g) at the atmospheric pressure in Test #2 for the heavy oil–CO_2 system.
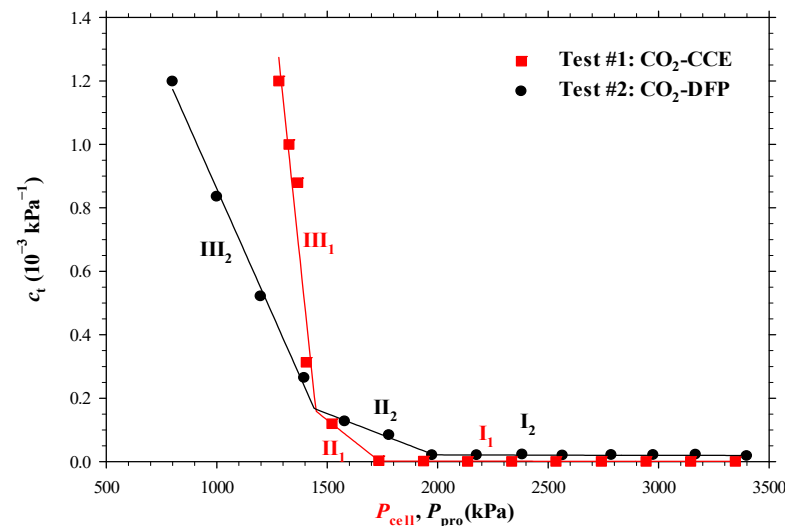
Figure 6. Measured total isothermal compressibilities (c_t) in Tests #1 and #2.

In the third regions of the two tests, the absolute slopes of the total isothermal compressibilities became much larger. This means that the system's compressibility started to be dominated by the evolved gas phase. Bubbles were liberated in the third region, though some free gas could already exist at the late stage of the second region [14]. In the numerical simulations of Test #2, the bubble liberation rate depended on the amount of bubbles in the foamy heavy oil. The reaction frequency factor (rff_1) for the bubble liberation in Test #2 was found to be 0.009 min^{-1}.

4.2. Heavy Oil–CH$_4$ System

The equilibrium R_v vs. P_{cell} data predicted by using the PR-EOS in the CMG-WinProp module, the non-equilibrium R_v vs. P_{cell} data predicted by using the CMG-STARS module and the measured non-equilibrium R_v vs. P_{cell} data in Test #3 for the heavy oil–CH$_4$ system are plotted in Figure 7. The equilibrium and non-equilibrium R_v vs. P_{cell} data were almost the same when the test pressure was higher than the bubble-point pressure P_b = 1.70 MPa of the heavy oil–CH$_4$ system since the test fluid was still in the liquid phase at $P_{cell} > P_b$. The two relative volumes started to deviate from each other at P_b. The predicted equilibrium R_v increased suddenly when the test pressure was reduced from 1.70 MPa to 1.50 MPa. With further pressure reduction, the increase in R_v with each pressure drop became larger and larger. Conversely, the measured or predicted non-equilibrium R_v was increased by less than 0.5% as the test pressure was decreased from 1.70 MPa to 1.50 MPa. As the test pressure continued to decrease, the non-equilibrium R_v was increased slightly with each pressure drop until P_{cell} = 0.70 MPa. This indicates that no gas was exsolved from the live heavy oil in the non-equilibrium CCE test until P_{cell} was 1 MPa lower than P_b. The measured or predicted non-equilibrium R_v was increased drastically when the test pressure was reduced from 0.70 MPa to 0.50 MPa. This was because a large number of bubbles were nucleated at P_{cell} = 0.50 MPa. The tuned rff_e in Test #3 was found to be 0.00009 min^{-1} in the CMG-STARTS module. The low rff_e in Test #3 indicated that the dissolved gas was exsolved from the live oil rather slowly, which was consistent with the high supersaturation measured in the test.
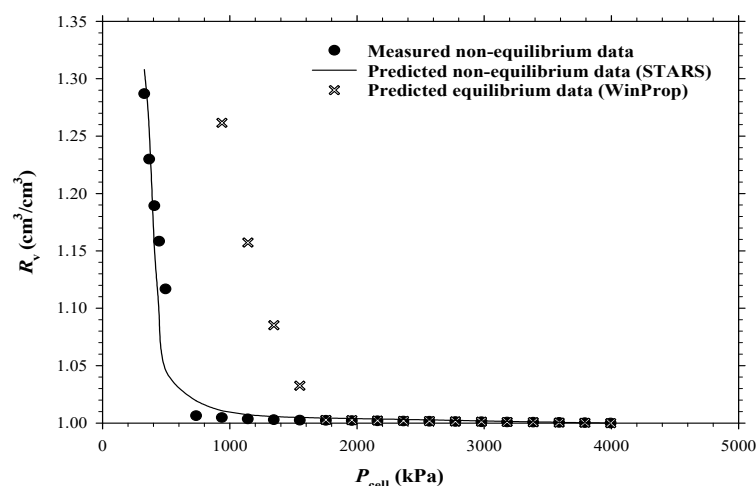

Figure 7. Measured and predicted non-equilibrium relative volume (R_v) vs. PVT cell pressure (P_{cell}) data as well as predicted equilibrium R_v vs. P_{cell} data in Test #3 for the heavy oil–CH$_4$ system.

The measured and predicted production data (P_e, Q_f, Q_o, Q_g) in Test #4 are depicted in Figure 8. It can be found from the history matching that the predicted cumulative total fluids production data had relatively larger deviations from the measured data at lower test pressures. The deviations of the predicted data from the measured data were also found at low test pressures in the CO$_2$-DFP test (Test #2). These deviations could be attributed to the measured cumulative total fluids production data (Q_f) at low pressures. The accuracy of Q_f measurements was compromised at a low pressure due to the large expansion of free gas in the separator at the low pressure. The overall production trends in the CH$_4$-DFP test (Test #4) were similar to those in the CO$_2$-DFP test (Test #2). The major difference was the cumulative oil productions (Q_o) in the two tests. In Test #2, the slope of Q_o vs. time data had an obvious decrease when P_n = 1.97 MPa was reached. In contrast, the slope of Q_o vs. time data in Test #4 was marginally increased once P_e was reduced below P_n. The slope remained almost the same for a long time before the free gas was produced. This could be because the exsolution of CH$_4$ from the live heavy oil did not significantly affect the foamy-oil viscosity [40].
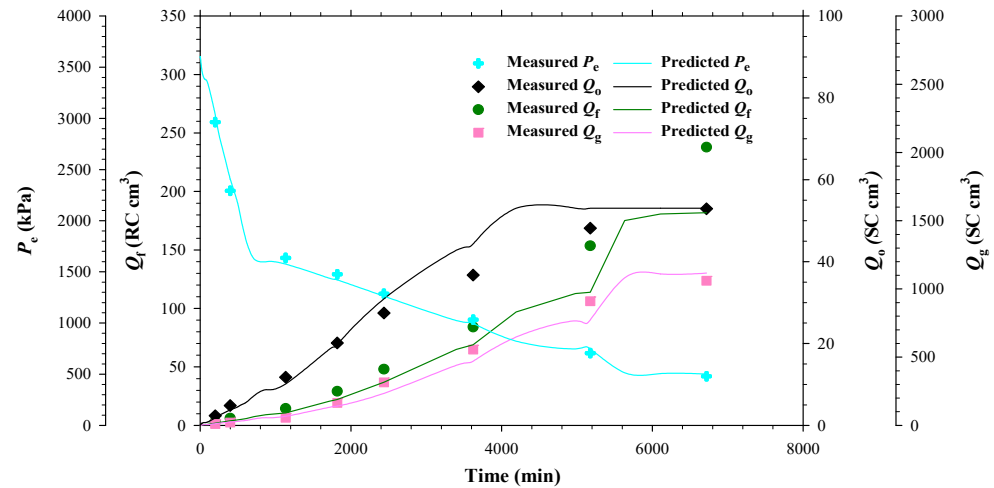
Figure 8. Measured and predicted pressures at the opposite end of the producer (P_e); cumulative total fluids production (Q_f) at the reservoir conditions; cumulative oil and gas productions (Q_o and Q_g) at the atmospheric pressure in Test #4 for the heavy oil–CH_4 system.

The measured total isothermal compressibilities (c_t) in Tests #3 and #4 are shown in Figure 9. Unlike the measured total isothermal compressibilities in Tests #1 and #2 as shown in Figure 6, the measured total isothermal compressibility data in Tests #3 and #4 only had one turning point in each dataset. This meant that CH_4 bubbles tended to be nucleated more instantaneously in comparison with CO_2 bubbles. The turning points in the two datasets in Figure 9 were $P_n = 0.60$ and 1.50 MPa in Tests #3 and #4, respectively. Therefore, the critical supersaturation at $P_n = 0.60$ MPa was $P_{crit} = 1.70 - 0.60 = 1.10$ MPa in Test #3, whereas the critical supersaturation at $P_n = 1.50$ MPa was $P_{crit} = 1.70 - 1.50 = 0.20$ MPa in Test #4. The large difference of the critical supersaturations in the two tests shows that the porous media strongly affect P_n and P_{crit} for the heavy oil–CH_4 system. In the numerical simulations for the two tests, the tuned rff_e in Test #3 (CH_4-CCE) was 0.00009 min^{-1}, which was much smaller than the tuned $rff_e = 0.013$ min^{-1} in Test #4 (CH_4-DFP). Hence, the numerical simulation results also show that the presence of the porous media can cause the dissolved gas to be exsolved more readily. The value of rff_1 in Test #4 was tuned to be 0.00019 min^{-1}. The high rff_e but low rff_1 for the heavy oil–CH_4 system in the porous media indicate that CH_4 is an excellent solvent to induce and maintain foamy-oil flow in the porous media.
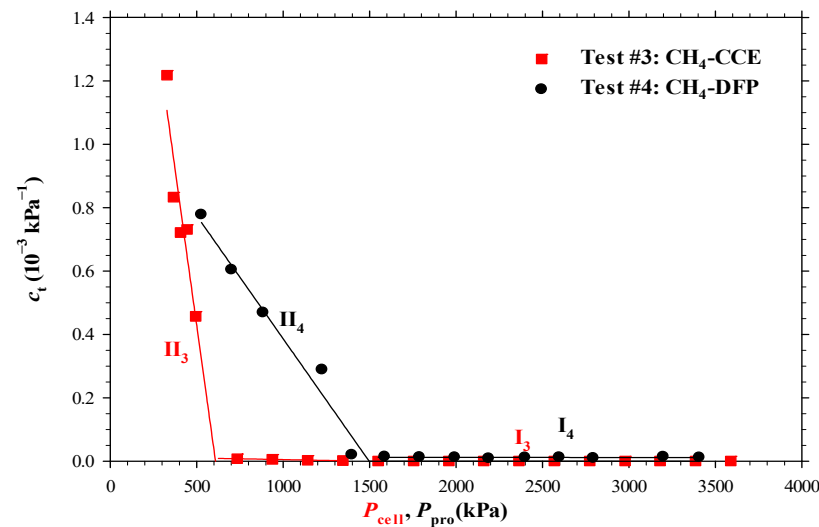
Figure 9. Measured total isothermal compressibilities (c_t) in Tests #3 and #4.

4.3. Heavy Oil–C₃H₈ System

Figure 10 compares the three different R_v vs. P_{cell} data for the heavy oil–C₃H₈ system: the predicted equilibrium data from the GMG-WinProp module; the measured non-equilibrium data from CCE test; and the predicted non-equilibrium data from the CMG-STARS module. This figure shows that, similar to the predicted equilibrium R_v vs. P_{cell} data in the other two heavy oil–solvent systems, the predicted equilibrium R_v data had a sudden increase once P_{cell} was decreased to P_b = 0.48 MPa. Both the measured and predicted non-equilibrium values of R_v were increased gradually after the pressure was decreased slightly below P_b. This fact means that the critical supersaturation required for the C_3H_8 bubbles to nucleate was lower than that for the CO_2 bubbles. As the test pressure was further reduced, the predicted equilibrium R_v increased quickly while the non-equilibrium R_v was increased rather slowly. This large deviation was caused by the low bubble nucleation rate and gas diffusion rate in the heavy oil [41]. The predicted R_v vs. P_{cell} data agreed well with the measured R_v vs. P_{cell} data. It was found in the numerical simulation results that a single rff_e did not give a satisfactory matching result. Therefore, two different rff_e values had to be used in two pressure ranges in the CMG-STARS module. Both values of rff_e were found to be rather low for the heavy oil–C_3H_8 system, 0.0001 min^{-1} in the test pressures of 0.50−0.40 MPa and 0.000065 min^{-1} in the test pressures of 0.40−0.30 MPa.
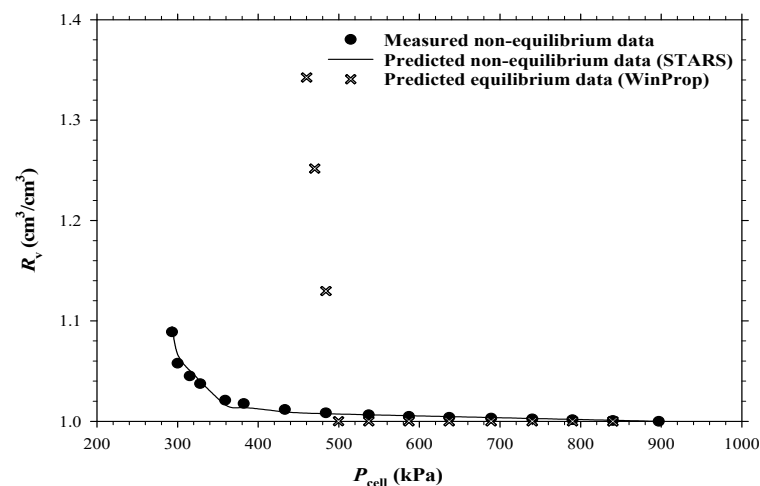

Figure 10. Measured and predicted non-equilibrium relative volume (R_v) vs. PVT cell pressure (P_{cell}) data as well as predicted equilibrium R_v vs. P_{cell} data in Test #5 for the heavy oil–C₃H₈ system.

The measured and predicted production data for Test #6 are plotted in Figure 11. The predicted data had a satisfactory agreement with the measured data with a global error of 8.2%. As shown in the figure, P_e had a similar trend to those in Tests #2 (CO₂-DFP) and #4 (CH₄-DFP). It decreased quickly at $P_e > P_n$ and much more slowly after the bubble started to nucleate. The tuned rff_e and rff_1 for Test #6 were found to be 0.00025 min^{-1} and 0.0045 min^{-1}. Figure 12 shows the total isothermal compressibilities (c_t) measured in Tests #5 and #6. Similar to the measured total isothermal compressibilities (c_t) in Tests #1 (CO₂-CCE) and Test #2 (CO₂-DFP), the measured c_t data in Tests #5 and #6 also had two turning points and three regions in each dataset. This suggests that C_3H_8 and CO_2 bubbles were nucleated more gradually than CH_4 bubbles. The pressures at the first turning points of the two datasets were the bubble-nucleation pressures (P_n). They were 480 kPa in Test #5 and 500 kPa in Test #6, which were close to and the same as P_b = 500 kPa. This means that the supersaturation in the heavy oil–C_3H_8 system is almost negligible, whether a test was conducted in the porous media or not. In comparison with the heavy oil–CO_2 system, the heavy oil–C_3H_8 system had lower rff_e values in the bulk phases and porous media. This indicates that gas was exsolved more slowly in the heavy oil–C_3H_8 system at the same supersaturation. In addition, the tuned rff_1 of 0.0045 min^{-1} in Test #6 with the porous media was also lower than rff_1 = 0.009 min^{-1} in Test #2 with the porous media.

Therefore, the heavy oil–C_3H_8 system had more stable foamy oil than that in the heavy oil–CO_2 system.
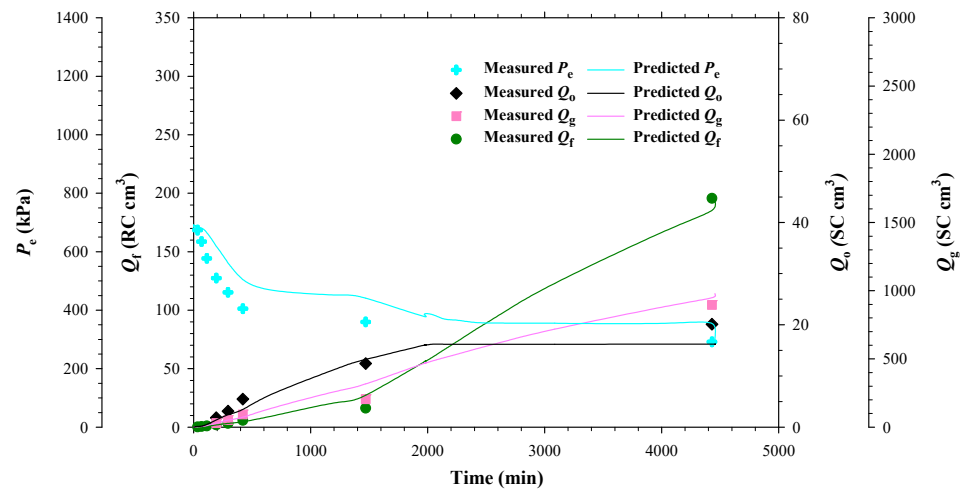
Figure 11. Measured and predicted pressures at the opposite end of the producer (P_e); cumulative total fluids production (Q_f) at the reservoir conditions; cumulative oil and gas productions (Q_o and Q_g) at the atmospheric pressure in Test #6 for the heavy oil–C_3H_8 system.
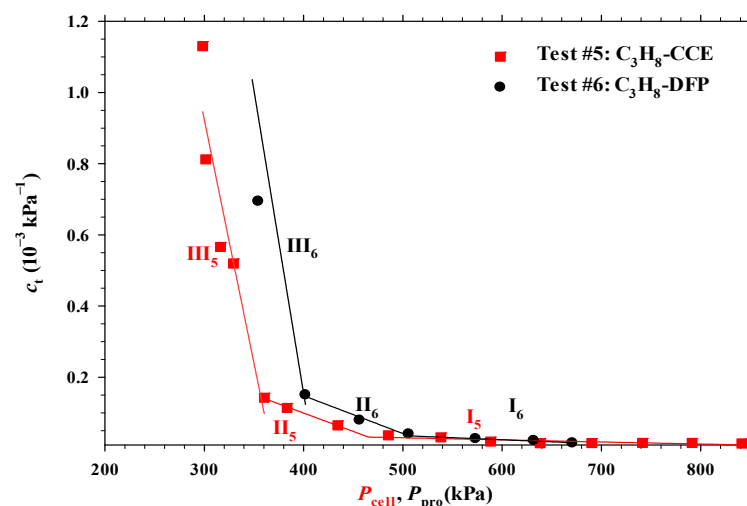
Figure 12. Measured total isothermal compressibilities (c_t) in Tests #5 and #6.

5. Conclusions

In this paper, the solvent exsolution and liberation processes of three different heavy oil–solvent systems in the porous media and bulk phases were studied experimentally and numerically. The following conclusions can be drawn from this study:

- The measured bubble-nucleation pressures (P_n) for the heavy oil–CO_2 system, heavy oil–CH_4 system and heavy oil–C_3H_8 system in the porous media were 0.24 MPa, 0.90 MPa and 0.02 MPa higher, respectively, than those in the bulk phases. This was because a lower supersaturation was needed for the bubble nucleation to occur in the porous media than that in the bulk phases.
- The measured total isothermal compressibility (c_t) vs. test pressure (P) data in the heavy oil–CH_4 system showed that the nucleation of CH_4 bubbles was found to be more instantaneous than that of CO_2 or C_3H_8 bubbles.
- Numerically, the obtained reaction frequency factors (rff_e) for the gas exsolution were all higher in the tests with the porous media than those with the bulk phases for the

three heavy oil–solvent systems. The higher rff_e indicated that the dissolved gas was more readily to be exsolved from the heavy oil.
- The reaction frequency factors (rff_1) for the gas liberation in the heavy oil–C_3H_8 system with the porous media was found to be lower than that for the heavy oil–CO_2 system, suggesting that the former system had more stable foamy oil than that in the latter system.
- The high rff_e but low rff_1 in the heavy oil–CH_4 system with the porous media showed that CH_4 was an excellent solvent for inducing and maintaining foamy oil in the porous media.

References

1. Maini, B.B. Foamy oil flow in heavy oil production. *J. Can. Pet. Technol.* **1996**, *35*, 21–24. [CrossRef]
2. Sheng, J.; Maini, B.; Hayes, R.; Tortike, W. Experimental study of foamy oil stability. *J. Can. Pet. Technol.* **1997**, *36*, 31–37. [CrossRef]
3. Wang, J.; Yuan, Y.; Zhang, L.; Wang, R. The influence of viscosity on stability of foamy oil in the process of heavy oil solution gas drive. *J. Pet. Sci. Eng.* **2009**, *66*, 69–74. [CrossRef]
4. Sheng, J.J.; Hayes, R.E.; Maini, B.B.; Tortike, W.S. Modelling foamy oil flow in porous media. *Transp. Porous Media* **1999**, *35*, 227–258. [CrossRef]
5. Wu, M.; Lu, X.; Yang, J.; Lin, Z.; Zeng, F. Experimental analysis of optimal viscosity for optimizing foamy oil behavior in the porous media. *Fuel* **2020**, *262*, 116602. [CrossRef]
6. Li, S.; Hu, Z.; Lu, C.; Wu, M.; Zhang, K.; Zheng, W. Microscopic visualization of greenhouse-gases induced foamy emulsions in re-covering unconventional petroleum fluids with viscosity additives. *J. Chem. Eng.* **2021**, *411*, 128411. [CrossRef]
7. Shi, W.; Ma, Y.; Tao, L.; Zhang, N.; Ma, C.; Bai, J.; Xu, Z.; Zhu, Q.; Zhong, Y. Study of the enhanced oil recovery mechanism and remaining oil state of heavy oil after viscosity-reducer-assisted CO_2 Foam flooding: 2D microvisualization experimental case. *Energy Fuels* **2023**, *32*, 18620–18631. [CrossRef]
8. Sun, X.; Cai, L.; Zhang, Y.; Li, T.; Song, Z.; Teng, Z. Comprehensive investigation of non-equilibrium properties of foamy oil induced by different types of gases. *Fuel* **2022**, *316*, 123296. [CrossRef]
9. Zhou, X.; Zeng, F.; Zhang, L.; Wang, H. Foamy oil flow in heavy oil–solvent systems tested by pressure depletion in a sandpack. *Fuel* **2016**, *171*, 210–223. [CrossRef]
10. Li, S.; Li, Z.; Wang, Z. Experimental study on the performance of foamy oil flow under different solution gas–oil ratios. *RSC Adv.* **2015**, *5*, 66797–66806. [CrossRef]
11. Zhou, X.; Yuan, Q.; Zeng, F.; Zhang, L.; Jiang, S. Experimental study on foamy oil behavior using a heavy oil–methane system in the bulk phase. *J. Pet. Sci. Eng.* **2017**, *158*, 309–321. [CrossRef]
12. Tang, G.-Q.; Firoozabadi, A. Gas- and liquid-phase relative permeabilities for cold production from heavy-oil reservoirs. *SPE Reserv. Evaluation Eng.* **2003**, *6*, 70–80. [CrossRef]
13. Modaresghazani, J.; Moore, R.; Mehta, S.; Anderson, M.; Badamchi-Zadeh, A. A novel method (CCE&C) to study transient phase behaviour in heavy oil and ethane. *Fuel* **2019**, *257*, 115946. [CrossRef]
14. Yao, J.; Zou, W.; Gu, Y. Solvent effects on the measured bubble-point pressures and pseudo bubble-point pressures of different heavy crude oil–solvent systems. *Petroleum* **2022**, *8*, 577–586. [CrossRef]
15. Dong, X.; Xi, Z.; Zadeh, A.B.; Jia, N.; Gates, I.D. A Novel Experimental Method CCEC and Modelling of Methane Dissolution and Exsolution in Heavy Oil. In Proceedings of the SPE 199942, Presented at the Canada Heavy Oil Conference, Calgary, AB, Canada, 29 September–2 October 2020.

16. Shi, Y.; Zhao, W.; Li, S.; Yang, D. Quantification of gas exsolution and preferential diffusion for alkane solvent(s)–CO2–heavy oil systems under nonequilibrium conditions. *J. Pet. Sci. Eng.* **2021**, *208*, 109283. [CrossRef]

17. Bauget, F.; Egermann, P.; Lenormand, R. A New model to obtain representative field relative permeability for reservoirs produced under solution-gas drive. *SPE Reserv. Evaluation Eng.* **2005**, *8*, 348–356. [CrossRef]

18. Uddin, M. Numerical studies of gas exsolution in a live heavy oil reservoir. In Proceedings of the SPE 97739, Presented at the International Thermal Operations and Heavy Oil Symposium, Calgary, AB, Canada, 1–3 November 2005.

19. Ivory, J.; Chang, J.; Coates, R.; Forshner, K. Investigation of cyclic solvent injection process for heavy oil recovery. *J. Can. Pet. Technol.* **2010**, *49*, 22–33. [CrossRef]

20. Zhou, X.; Zeng, F.; Zhang, L.; Jiang, Q.; Yuan, Q.; Wang, J.; Zhu, G.; Huang, X. Experimental and mathematical modeling studies on foamy oil stability using a heavy oil–CO_2 system under reservoir conditions. *Fuel* **2020**, *264*, 116771. [CrossRef]

21. Shahvali, M.; Pooladi-Darvish, M. Dynamic modelling of solution-gas drive in heavy oils. *J. Can. Pet. Technol.* **2009**, *48*, 39–46. [CrossRef]

22. Sun, X.; Zhang, Y.; Wang, S.; Song, Z.; Li, P.; Wang, C. Experimental study and new three-dimensional kinetic modeling of foamy solution-gas drive processes. *Sci. Rep.* **2018**, *8*, 4369. [CrossRef]

23. Arora, P.; Kovscek, A.R. A mechanistic modeling and experimental study of solution gas drive. *Transp. Porous Media* **2003**, *51*, 237–265. [CrossRef]

24. Ma, H.; Yu, G.; She, Y.; Gu, Y. A new hybrid production optimization algorithm for the combined CO_2-cyclic solvent injection (CO_2-CSI) and water/gas flooding in the post-CHOPS reservoirs. *J. Pet. Sci. Eng.* **2018**, *170*, 267–279. [CrossRef]

25. Li, Q.; Wang, Y.; Owusu, A.B. A modified Ester-branched thickener for rheology and wettability during CO_2 fracturing for im-proved fracturing property. *Environ. Sci. Pollut. Res.* **2019**, *26*, 20787–20797. [CrossRef] [PubMed]

26. Li, Q.; Liu, J.; Wang, S.; Guo, Y.; Han, X.; Li, Q.; Cheng, Y.; Dong, Z.; Li, X.; Zhang, X. Numerical insights into factors affecting collapse behavior of horizontal wellbore in clayey silt hydrate-bearing sediments and the accompanying control strategy. *Ocean Eng.* **2024**, *297*, 117029. [CrossRef]

27. Coombe, D.; Maini, B. Modeling Foamy Oil Flow. In *Workshop on Foamy Oil Flow*; Petroleum Recovery Institute: Calgary, AB, Canada, 1994.

28. Bayon, Y.M.; Cordelier, P.R.; Nectoux, A. A new methodology to match heavy-oil long-core primary depletion experiments. In Proceedings of the SPE 75133, Presented at the Improved Oil Recovery Conference, Tulsa, OK, USA, 13–17 April 2002.

29. Ma, H.; Huang, D.; Yu, G.; She, Y.; Gu, Y. Combined cyclic solvent injection and waterflooding in the post-cold heavy oil production with sand reservoirs. *Energy Fuels* **2017**, *31*, 418–428. [CrossRef]

30. Yao, J.; Zou, W.; Gu, Y. Experimental and theoretical studies of solvent bubble nucleation and liberation processes in different heavy crude oil–solvent systems. *J. Pet. Sci. Eng.* **2022**, *217*, 110949. [CrossRef]

31. Oskouei, S.J.P.; Zadeh, A.B.; Gates, I.D. A new kinetic model for non-equilibrium dissolved gas ex-solution from static heavy oil. *Fuel* **2017**, *204*, 12–22. [CrossRef]

32. Brooks, R.H.; Corey, A.T. Hydraulic properties of porous media and their relation to drainage design. *T ASAE* **1964**, *7*, 26–28.

33. Computer Modelling Group (CMG) Ltd. *STARS Users' Guide*; Computer Modelling Group (CMG) Ltd.: Calgary, AB, Canada, 2016.

34. Chen, T.; Leung, J.Y.; Bryan, J.L.; Kantzas, A. Analysis of non-equilibrium foamy oil flow in cyclic solvent injection processes. *J. Pet. Sci. Eng.* **2020**, *195*, 107857. [CrossRef]

35. Wang, H.; Torabi, F.; Zeng, F. Investigation of non-equilibrium solvent exsolution dynamics and bubble formation and growth of a CO_2/C_3H_8/heavy-oil system by micro-optical visualizations: Experimental and continuum-scale numerical studies. *Fuel* **2023**, *332*, 126188. [CrossRef]

36. Albartamani, N.S.; Ali, S.F.; Lepski, B. Investigation of foamy oil phenomena in heavy oil reservoirs. In Proceedings of the SPE 54084, Presented at the International Thermal Operations and Heavy Oil Symposium, Bakersfield, CA, USA, 17–19 March 1999.

37. Sahni, A.; Gadelle, F.; Kumar, M.; Tomutsa, L.; Kovscek, A.R. Experiments and Analysis of Heavy-Oil Solution-Gas Drive. *SPE Reserv. Eval. Eng.* **2004**, *7*, 217–229. [CrossRef]

38. Wang, H.; Zeng, F.; Torabi, F.; Xiao, H. Experimental and numerical studies of non-equilibrium solvent exsolution behavior and foamy oil stability under quiescent and convective conditions in a visualized porous media. *Fuel* **2021**, *291*, 120146. [CrossRef]

39. Bryan, J.; Butron, J.; Nickel, E.; Kantzas, A. Measurement of Non-Equilibrium Solvent Release from Heavy Oil during Pressure Depletion. In Proceedings of the SPE Canada Heavy Oil Conference, Calgary, AB, Canada, 13–14 March 2018.

40. Alshmakhy, A.; Maini, B.B. Foamy-oil-viscosity measurement. *J. Can. Pet. Technol.* **2012**, *51*, 60–65. [CrossRef]

41. Yang, C.; Gu, Y. Diffusion coefficients and oil swelling factors of carbon dioxide, methane, ethane, propane, and their mixtures in heavy oil. *Fluid Phase Equilibria* **2006**, *243*, 64–73. [CrossRef]